Journal of Materials Chemistry B

ROYAL SOCIETY OF CHEMISTRY

PAPER

View Article Online
View Journal | View Issue

Cite this: J. Mater. Chem. B, 2025, 13, 9498

Two photon-responsive gold nanocapsules enable targeted photothermal hyperthermia of chemoresistant melanoma: injection-route-dependent efficacy and renal evidence of fragment clearance†

Paula Zamora-Pérez,‡[a] Qiutian She,‡[a] Harrisson D. Santos,[b] Jose J. Conesa,[c] M. Carmen Iglesias de la Cruz,[b] Nuria Fernández,[b] Daniel Jaque [b] and Pilar Rivera-Gil *[a]

Melanoma is a highly aggressive skin cancer that often develops resistance to chemotherapy, underscoring the need for new treatment strategies. Here we evaluate plasmonic gold nanocapsules (AuNCs) as photoresponsive agents for two-photon luminescence-assisted photothermal therapy in chemoresistant melanoma models. The performance of the AuNCs was assessed in two-dimensional cell cultures, three-dimensional paclitaxel-resistant B16-F10 melanoma spheroids, and a subcutaneous melanoma mouse model under near-infrared excitation. *In vitro*, AuNCs alone exhibited no cytotoxicity, but under 830 nm two-photon excitation, they produced strong two-photon luminescence and thermal effects that increased with nanocapsule concentration and laser power. This led to transient oxidative stress, apoptosis induction, and effective melanoma cell ablation under optimal conditions (80 μg mL^{-1} AuNCs, 12 mW laser power). *In vivo*, the route of nanoparticle administration proved decisive. A single 4-min 806 nm irradiation after intratumoral injection uniformly heated the lesion (≈45–50 °C), yielded durable tumour eradication, and sequestered >99% of detected gold in the necrotic scab, with only trace renal clearance. In contrast, the same laser fluence after peritumoral injection generated a superficial hot rim, spared the tumour core, allowing eventual regrowth, and left ~65% of the injected gold systemically redistributed, mainly in the spleen and liver. These findings highlight the potential of AuNCs as potent, image-guided photothermal agents for chemoresistant melanoma, offering targeted tumor destruction with limited systemic exposure. They reveal the injection route is a critical determinant of both therapeutic success and nanoparticle biodistribution.

Received 23rd January 2025,
Accepted 16th June 2025

DOI: 10.1039/d5tb00167f

rsc.li/materials-b

Introduction

Cutaneous malignant melanoma accounts for ≤1% of skin cancers yet it is responsible for most related deaths. Globocan 2022 recorded 331 722 new cases and 58 667 deaths worldwide.[1] Independent burden of disease studies confirm the rising incidence while attributing a substantial proportion to ultraviolet radiation exposure.[2–4] Surgical excision cures most stage I tumors, but once distant metastases develop, the 5-year survival rate falls below 15%.[5] Immune-checkpoint inhibitors (ICIs) targeting CTLA-4, PD-1 and, more recently, the LAG-3 antibody relatlimab in combination with nivolumab, have revolutionized melanoma therapy.[6,7] Furthermore, autologous tumor-infiltrating lymphocyte therapy has entered the clinic.[8] Nevertheless, primary or acquired resistance occurs in ~50% of patients and immune-related adverse events can be severe.[9,10] For tumors harboring BRAF-V600 mutations, combined BRAF/MEK inhibition achieves high initial responses, but durable remissions remain uncommon and systemic toxicity limits chronic use.[9] Chemotherapy and external-beam radiotherapy remain largely palliative because melanoma is intrinsically chemo- and radio-resistant. These limitations demand tumor-selective local treatments that eradicate residual disease while synergizing with systemic immunity.

[a] Integrative Biomedical Materials and Nanomedicine Lab, Department of Medicine and Life Sciences (MELIS), Pompeu Fabra University, PRBB, Carrer Doctor Aiguader 88, 08003 Barcelona, Spain. E-mail: pilar.rivera@upf.edu
[b] Fluorescence Imaging Group, Departamento de Física de Materiales, Universidad Autónoma de Madrid, C/Francisco Tomás y Valiente 7, 28049 Madrid, Spain
[c] Mistral Beamline, Experiment Division, ALBA Synchrotron (ALBA-CELLS), Barcelona, Spain

† Electronic supplementary information (ESI) available. See DOI: https://doi.org/10.1039/d5tb00167f

‡ Equally contributing authors.

Photothermal therapy (PTT) offers an orthogonal physical modality that converts NIR light into cytotoxic heat localized to the tumor, while priming systemic antitumor immunity through immunogenic cell death. Hyperthermia kills cancer cells by raising the tumor temperature above a physiological level.[11,12] Heat disrupts the endoplasmic reticulum and mitochondria homeostasis, drives reactive oxygen species (ROS) production and elicits ROS-driven apoptosis and ER stress-mediated cell death.[13,14] Because melanomas already harbour elevated ROS due to melanin synthesis,[15] an acute ROS surge is particularly cytotoxic. Local heat further boosts antitumour immunity by releasing tumor-associated antigens, promoting immunogenic cell death (ICD),[16,17] improving blood flow and vascular permeability, and recruiting immune effector cells.[18] Conventional ''outside-in'' heating with radiofrequency or microwave applicators produces centimeter-scale isotherms that can harm adjacent healthy tissue, limiting its clinical utility.[19–22] Nanotechnology allows an ''inside-out'' approach: stimuli-responsive nanoparticles accumulate in the tumor and convert external physical energy (light, alternating magnetic fields, ultrasound or radiofrequency) into heat with sub-millimeter precision.[20] Gold–silica nanoshells provided the first proof-of-concept for *in vivo* nPTT two decades ago[23] and inspired a broad range of other photothermal nanomaterials such as semiconducting polymers,[24] copper sulfide,[25] FDA-listed Prussian-blue,[26] and black-phosphorus quantum dots.[27] Among the available nanoplatforms, gold nanoparticles,[28,29] iron-oxide,[30] or silica are commonly used in hyperthermia and stand out due to their biocompatibility and powerful photothermal performance.[31–33]

Regarding melanoma treatment, the most suitable approach for external small superficial lesions is NIR-induced NP-assisted PTT (nPTT),[28,34,35] while deeper lesions may benefit from radiofrequency, magnetic or ultrasound heating.[20] AuNPs are the best candidates for nPTT because of their facile and controlled synthesis, easy optical property tunability, targetability[36] and biofunctionalization, loading capabilities, cellular uptake, and safe biological profile.[37–42] At the nanoscale, collective surface-electron oscillations give rise to localized surface plasmon resonance (LSPR).[43–45] Spectroscopy tracking of the LSPR predicts photothermal efficiency.[46,47] Excitation in the ''biological'' NIR window (700–980 nm) maximizes tissue penetration, while two-photon excitation (2PE) of AuNPs additionally generates intrinsic luminescence for image-guided therapy.[48–50] Besides, AuNPs can induce ROS-mediated cell death for photodynamic therapy (PDT).[29,51–56] Singh *et al.* developed NIR-II-active, capsule-shaped, and rattle-like bimetallic nanoparticles, which exhibited excellent photothermal efficiency at low power density by using an NIR-II laser (1064 nm), affirming the photothermal efficacy of nanocapsules.[31] Li *et al.* designed carbon–silica nanocapsules with gold nanoparticles inside the cavity. These multifunctional nanocapsules exhibiting excellent photothermal conversion and good biocompatibility achieved a synergistic effect between photothermal- and chemo-therapy.[32] Grabowska-Jadach *et al.* reported plasmonic hollow gold nanoshells modified with aptamers selective towards nucelolin for the photothermal treatment of skin cancer. Their hollow gold nanoshells exhibited good water solubility, colloidal stability during modification and purification stages, as well as an LSPR band in the NIR region.[33]

Mechanistic studies show that plasmonic heat triggers membrane disruption, protein denaturation and oxidative stress[57] and that sub-lethal hyperthermia promotes ICD, augmenting antigen presentation and synergizing with PD-1 blockade in melanoma models.[58,59] Early clinical trials have confirmed the safety of nPTT in prostate (silica–gold nanoshells; NCT02680535).[19] This trial demonstrates the clinical feasibility of intratumoral nanoparticle delivery and NIR laser parameters comparable to ours.

We previously engineered hollow ~400 nm gold nanocapsules (AuNCs) by layer-by-layer deposition of polyelectrolytes and gold seed on silica templates followed by core dissolution and gold growth.[29,60–62] The plasmonic surface exhibits broadband extinction across the first NIR window and converts 830 nm 2PE into heat with ~37% efficiency, outperforming mass-matched nanorods or nanostars. Their internal cavity can host diagnostic or therapeutic cargoes, providing true theranostic capacity, while intrinsic two-photon luminescence (2PL) enables μm-scale tracking under clinically permissible NIR fluences. Importantly, their synthesis uses clinical-grade reagents and yields endotoxin-free dispersions, facilitating translation.

Here we exploit the dual imaging and heating functionality of AuNCs to eradicate multi-drug-resistant melanoma. In paclitaxel-resistant B16-F10 spheroids, a single 10 min 2PE pulse (830 nm, 12 mW) delivered with 80 μg mL^{-1} AuNCs generates abundant ROS, perforates the plasma membrane, and kills >90% of cells, whereas AuNCs or laser alone are innocuous.[29] Cryo-soft X-ray tomography confirms AuNC fragmentation and μm-scale membrane pores, consistent with inside-out-hyperthermia. Translating these parameters to murine B16-F10 xenografts, a single 4-min 806 nm exposure following intratumoral (IT) AuNC delivery raises the entire lesion to a temperature of 45°–50 °C, achieves complete remission in all animals, and confines >99% of the injected gold within the necroric scab that is later shed. In contrast, peritumoral (PT) injection yields a superficial ''hot rim'', leaves the core viable, allows regrowth, and redistributes ≈65% of the AuNCs to the liver and spleen. Thus, the injection route critically determines both therapeutic outcome and systemic nanoparticle burden.

Importantly, longitudinal studies are beginning to clarify the fate of residual gold and its immunological footprint. Dextran-coated 21 nm AuNPs persist in murine liver and spleen for at least two weeks yet cause no histopathological alterations or elevations in serum transaminases, creatinine or IL-6, arguing against chronic hepato- or nephron-toxicity.[63] A comparative toxicology screen in C57BL/6 mice found that AuNPs transiently elevate IL-6 and TNF-α and expand memory $CD8^+$ T-cells within 2 h, but all cytokine and activation markers return to baseline by 96 h, suggesting a self-limited innate response with potential adjuvant benefit.[64] Particle engineering can further mitigate organ retention: glutathione-protected ultrasmall $Au_{(25)}$ nanoclusters achieve 36% renal clearance within 24 h and >90% overall elimination by 28 days, whereas albumin-coated analogues retain >95% of gold in

mononuclear-phagocytic system organs and prolong cytokine activation.[65] Notably, our IT protocol sequesters >99% of AuNCs in the desquamated eschar, virtually abolishing off-target accumulation. Collectively, these data support a broad therapeutic window and indicate that residual gold deposits are largely immunologically inert, or even mildly immunostimulatory, when particle size, surface chemistry and administration route are optimized.

AuNC-mediated nPTT therefore emerges as a single session, image-guided strategy for hyperthermia eradication of drug-resistant melanoma while minimizing systemic, off-target exposure. Given its capacity for cargo loading, the platform provides a rational foundation for combining local hyperthermia with ICIs or encapsulated chemotherapeutics, and the mechanistic insights obtained here will inform the broader clinical translation of IT nanomedicines.

Experimental

Synthesis and characterization of gold nanocapsules

Synthesis. We followed a previously reported protocol[60,66] for the synthesis of AuNCs with some modification to enhance the plasmonic surface.[61,62] AuNCs were synthesized using a layer-by-layer (LbL) templating approach. Briefly, polystyrene (PS) beads (400 nm in diameter) served as templates and were alternately coated with negatively charged poly(styrene sulfonate) (PSS) and positively charged poly(allylamine hydrochloride) (PAH) to build up multilayers, terminating with a dense outer layer of PAH. Subsequently, a large excess of negatively charged gold seeds (2–3 nm in diameter, Au seeds) was electrostatically adsorbed onto the positively charged LbL surface, forming PS@Au-seed structures. These were thoroughly washed to remove unbound particles. To stabilize the structure, a polyvinylpyrrolidone (PVP) coating was applied, followed by the deposition of a silica shell. The PS cores were then dissolved using an ethanol/chloroform mixture, yielding hollow silica nanocapsules embedded with gold seeds. To enhance the plasmonic properties, the gold seeds were grown *in situ* by reducing gold ions with formaldehyde, using the pre-adsorbed seeds as nucleation sites, designated as gold nanocapsules (AuNCs). Silica-coated AuNCs were placed in Milli-Q water under stirring at RT for 48 h and washed three times with Milli-Q water for silica dissolution. The AuNCs were stored at 4 °C. No strong etchants, elevated temperatures or organic solvents were required, and the final capsules retained the ~400 nm diameter dictated by the original PS template while exhibiting the broadband plasmonic response characteristic of a contiguous metallic layer.

Rhodamine B-loaded AuNCs (RhoB-AuNCs) were synthesized using the same LbL protocol described above, with the modification of employing a fluorescent PS template. The fluorescent PS spheres were prepared by radical polymerization. Briefly, 0.15 g of polyvinylpyrrolidone (PVP, MW 55 000 kDa) and 0.128 g of 2,2′-azobis[2-(2-imidazolin-2-yl)propane]dihydrochloride (AIBA) were dissolved in 50 mL of argon-purged Milli-Q water. The solution was heated to 70 °C under reflux. After 5 g of styrene monomer was added, 15 mg of rhodamine B (Sigma-Aldrich) was introduced 5 minutes later, and the polymerization was allowed to proceed for 24 hours. The resulting fluorescent particles were collected by centrifugation at 9500 rpm for 30 minutes and washed three times with Milli-Q water. More details of the procedure are included in our previously published work.[36]

Transmission electron microscopy (TEM). The nanomaterials were diluted 1000× from the stock solution with ethanol, sonicated, and then, 10 μL were placed in a copper grid for visualization with an electron microscope (Phillips CM100).

Extinction spectra. The rest of the sample was used to measure the UV-vis extinction spectrum using a spectroscope (Ultrospec 2100 Pro).

Hyperspectral-enhanced dark-field microscopy (HEDFM). Optical scattering spectra of individual AuNCs were recorded with a CytoViva HEDFM 150 system (CytoViva Inc., Auburn, AL, USA). We used an illumination NA = 0.8 and a 60× oil objective. The HEDFM system consists of an Olympus BX51 microscope with a dark field condenser mounted and coupled to a spectrograph "V10E 2/3" attached to a CCD Imperx IPX-2M30 camera. The hyperspectral system collects the light scattered by the samples every 2 nm in the wavelength range of 400–1000 nm. The technique and its application to plasmonic shells are detailed in our previous work.[46,47,67]

The thermographic measurements of AuNCs in solution were performed under 806 nm excitation with a single-photon laser and images were recording with a FLIR thermocamera. For more details on the physicochemical properties of the NCs, please check our previous publication.[29]

Laser set-ups

Laser	Purpose (figures)	λ (nm)	Regime	Beam/scan geometry	Average power at sample	Key dosimetry parameters*
Ti:Sa pulsed (Spectra-Physics MaiTai eHP DeepSee on Leica SP5): Pulse energy = 38–150 pJ; peak power (P_{peak}) = 0.47–1.9 kW Time-averaged voxel irradiance (after duty-cycle $\approx 3.8 \times 10^{-6}$) = 21–84 W cm^{-2} Voxel dose over 60 s = 1–5 kJ cm^{-2}	2 PE imaging/*in vitro* nPTT (Fig. 2 and 3 and Fig. S1C, S2, S5, S6, ESI†)	830	80 fs, 80 MHz	Diffraction-limited focal spot, d = 0.264 μm (NA = 1.1 water). Raster-scanned 512 × 512 frame, 2 μs pixel dwell, 60 s total	3–12 mW	Instantaneous focal irradiance (I, W cm^{-2}) = (5.5–22) × 10^6

Table (*continued*)

Laser	Purpose (figures)	λ (nm)	Regime	Beam/scan geometry	Average power at sample	Key dosimetry parameters*
Diode (Lumics LU0806T040)	Photothermal efficiency curves (Fig. 1D and Fig. S8 right, ESI[1]†)	806	Continuous wave (CW)	3 mm collimated beam on cuvette	30 mW (1 W cm^{-2})	(1 W cm^{-2}; 6 min) → 360 J cm^{-2}
CW diode (Lumics LU0806T040)	*In vivo* nPTT (Fig. 4 and Fig. S7, S8 left, S9, S10,ESI[1]†)	806	CW	15 mm defocused spot on tumour	1.8 W (1 W cm^{-2})	(1 W cm^{-2}; 4 min) → 240 J cm^{-2}

Irradiance values are quoted in W cm^{-2} following hyperthermia-reporting guidelines. For the pulsed Ti:Sa source the instantaneous figures refer to the 264 nm focal spot; the time-averaged values account for galvo scanning (duty-cycle $\approx 3.8 \times 10^{-6}$).

830 nm (2PE, *in vitro*) and 806 nm (single-photon, AuNCs bulk and *in vivo*) lie on the same broadband LSPR shoulder of AuNCs, and no change in extinction is observed between 800 and 840 nm (Fig. 1C).

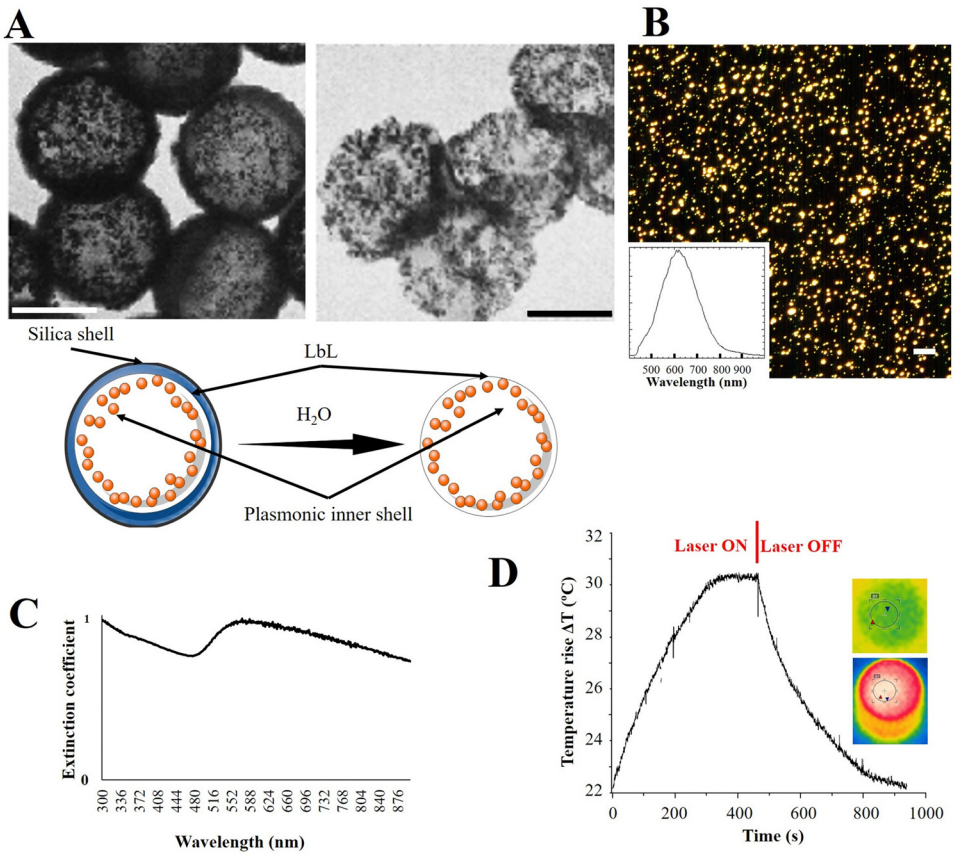

Fig. 1 Physico-chemical characterisation of gold nanocapsules (AuNCs). (A) Synthetic concept and TEM validation. A schematic (centre) depicts the layer-by-layer (LbL) adsorption of citrate-stabilised Au nanoparticles onto the inner wall of a sacrificial silica sphere, followed by dissolution of the template to yield a hollow plasmonic shell. TEM micrographs show a silica-coated AuNC (left) and the same capsule after silica removal (right), confirming preservation of the continuous metallic shell. Scale bar, 400 nm. (B) Hyperspectral-enhanced dark-field microscopy (HEDFM). The dark-field image reveals a uniform population of bright-scattering capsules; the overlaid mean spectrum (inset) displays a localised surface-plasmon maximum at ≈620 nm, attesting to narrow size distribution and excellent colloidal stability. Scale bar, 10 μm. (C) Optical extinction. The UV-visible absorbance profile of an aqueous AuNC dispersion exhibits a broad band that spans the visible and NIR windows, characteristic of strong inter-particle coupling within the hollow shell. (D) Photothermal performance. Bulk temperature of the dispersion recorded during continuous 806 nm laser irradiation (1 W cm^{-2}) rises by ~9 °C within 6 min and returns to baseline once the laser is switched off, illustrating efficient light-to-heat conversion. The initial temperature for all samples was 22 °C. Representative infrared thermographs before irradiation (upper inset) and at the temperature peak (lower inset) confirm homogeneous heating. Abbreviations: AuNCs, gold nanocapsules; HEDFM, hyperspectral-enhanced dark-field microscopy; LbL, layer-by-layer assembly.

Photothermal efficiency

The photothermal efficiency (η) of AuNCs under laser irradiation at 806 nm was obtained by applying the Wang model. In this model a certain mass (M) of the solution containing the photothermal agents is excited with an infrared (806 nm) laser. The time evolution of the solution temperature is measured until a steady state is achieved and the temperature increment (ΔT) is determined. Then, the heating laser is tuned off and the thermal relaxation of the solution is recorded to determine its thermal relaxation time (τ_s). In a first order approximation the laser-to-heat conversion efficiency is given by:[68]

$$\eta = \frac{M \cdot C \cdot \Delta T}{P_{abs} \cdot \tau_s} \quad (1)$$

where C is the heat capacity per unit mass of solution (2.43 J g^{-1} K^{-1} for the case of ethanol) and P_{abs} is the laser power absorbed by the solution. In this work the photothermal conversion efficiency was calculated by heating a solution of AuNCs in ethanol with an 806 nm continuous wave laser and recording the time evolution of the temperature of the solution with a thermal camera.

Cell culture

For cellular studies, B16-F10 mouse melanoma adherent cells were cultured in high glucose (4500 mg L^{-1}) Dulbecco's modified Eagle's medium (Gibco), supplemented with 1% penicillin–streptomycin (Hyclone) and 10% fetal bovine serum, FBS (Sigma Aldrich). Cells were cultured at 37 °C under a wet, modified atmosphere with 5% CO_2. B16-F10 melanoma spheroids obtained from serum-free B16-F10 adherent cells were seeded at a concentration of 750 cells per well in low-attachment 96-well plates (Corning) and cultured for 5 days in a supplemented Mammocult Human Medium Kit (STEMCELL technologies).[29] From the maximum projections, ROIs for each individual spheroid were performed.

In vitro characterization: Cell viability and cellular sensitivity to paclitaxel

Paclitaxel (PTX) was dissolved in ethanol, before mixing it with the cell medium. We prepared a PTX working solution of 50 μM.

(i) Cells were cultured as before. Trypan Blue staining was used to count (Countess™, C10228, Invitrogen™) the cells and to differentiate between live and dead cells in suspension. Live cells are impermeant to trypan blue and only enter the cell if the plasma membrane is damaged, thus being an indicator for cellular toxicity. Cells were treated for 24 h with PTX at different concentrations, 0.1–100 μM. As a control for viability, we used untreated cells. Then, we collected the cells by trypsinization of the adherent cells. We realized there were dead cells floating in the medium, therefore we also collected the medium from each well of the plate. Dead cells were stained with trypan blue (10 μL was added to 10 μL of cell medium). The viability was measured in % of the total amount of cells.

(ii) B16-F10 melanoma spheroids were incubated with PTX and AuNCs. Cell viability was measured using CytoCalcein violet 450 and propidium iodide, the total counts for each spheroid were obtained dividing the signal by the area of the spheroid. Mean ± SD were provided. ROS_{cyt} and apoptosis studies were performed in spheroids exposed to 30 μg mL^{-1} of AuNCs for 24 h, and treated with 6 μM CellROX deep red (Invitrogen) and with 10 μM apopxin (Abcam) for 1 h.

Nanocapsules. Our previous studies have already demonstrated the NCs' lack of toxicity.[29] Nevertheless, we confirmed it again. B16-F10 were seeded at a density of 2×10^5 cells in 2 mL of cell culture growth medium (GM). The cells were incubated at 37 °C with 5% CO_2 for 24 h.

Meanwhile we sterilized an aliquot of the NC dispersion. The aliquot was centrifuged at 8500 rpm for 30 minutes. After centrifugation the supernatant was removed, the same amount of sterile Milli-Q water was added and a sterile new Eppendorf was used. The entire process was repeated 3 times. The cells were incubated with 80 μg mL^{-1} NCs for 24 h and the viability was measured with trypan blue as described before.

Imaging was performed with a Leica SP5 confocal microscope using a 40× water immersion objective. The images of the tumor spheres were acquired with an Andor Dragonfly 500 spinning disk confocal microscope using a 40× water immersion objective. A region of interest (ROI) for each spheroid was obtained in the maximum projection, and the cell viability was calculated considering the total count per spheroid of propidium iodide and CytoCalcein violet 450 signals divided by the area of the spheroid obtained with FIJI. ROS and apoptosis studies were performed using 3D melanoma spheroids grown for 5 days; the spheroids were exposed for 24 h to 30 μg mL^{-1} of AuNCs, treated with 6 μM CellROX green and/or CellROX deep red (Invitrogen) with 10 μM apopxin (Abcam), and incubated for 1 h.

NC-mediated heat production. Cells were seeded as described before in the laser chamber and were incubated with 1, 10, and 80 μg mL^{-1} NCs. The distance to the laser was estimated to be between 6.5 to 7 cm to ensure the laser was focusing the NCs. The cells were irradiated with a 2-photon laser. Then cell viability was measured.

Concomitant treatment (PTX and heat). Cells were seeded as described before and treated with 0,1, 1, 2.5, 5, and 7.5 μM PTX. For this concomitant treatment strategy, we used 80 μg mL^{-1} NCs. The cells were cultured for 24 h and irradiated with an 806 nm laser following the previous protocol[69] at 12 mW for 10 minutes. We measured cell viability using trypan blue as previously described.

In vitro nPTT

The treatment of chemoresistant B16 melanoma spheroids was performed with a titanium sapphire multiphoton laser coupled to a Leica SP5 confocal microscope (830 nm) (see the laser set up section above).

The cryoSXT study was performed in B16 melanoma adherent cells seeded on Au-EM grids coated with holey carbon (R 2/2; Quantifoil) controlled so that 1–3 cells per grid square were obtained. Then, the cells were incubated for 24 h at 37 °C in a wet atmosphere and 5% CO_2 before adding the AuNCs at a

concentration of 30 μg mL^{-1}. After that, the grids with control and AuNC-treated cells were incubated for 10 min with LysoTracker green (1000×), washed with PBS 1x and vitrified by plunge-freezing them using a Leica EM GP unit. The samples were maintained in liquid nitrogen until visualization. Samples were imaged in cryo-conditions first using an epifluorescence microscope (integrated in the X-ray microscope) and afterwards with a soft X-ray microscope (at the Mistral beamline, ALBA). Based on the FL signal, the cell candidates were selected. Then, 2D mosaics were acquired to assess sample quality and the best candidates were acquired at a photon energy of 520 eV from −65° to 65° at 1° intervals (exposure time: 1–3 seconds). The tilt series of images were normalized with the XMIPP 3 software package,[70] aligned and reconstructed using IMOD.[71] For a more detailed protocol read the work by Chiappi *et al.* 2016.[72]

Synchrotron cryo-soft X-ray microscopy

A CryoSXT study was performed in B16-F10 melanoma adherent cells seeded onto Au-EM grids coated with holey carbon (R 2/2; Quantifoil) so that 1–3 cells per grid square were obtained. The cells were then incubated for 24 h at 37 °C in a wet atmosphere and 5% CO_2 before adding the AuNCs at a concentration of 30 μg mL^{-1}. When necessary, the cells were irradiated with an 806 nm laser at 3 mW. Subsequently, the grids with control and AuNC-treated cells were incubated for 10 min with LysoTracker green (1000×), washed with PBS 1×, and vitrified by plunge-freezing using a Leica EM GP unit. The samples were maintained in liquid nitrogen until visualization. The samples were imaged under cryo-conditions first with an epifluorescence microscope (integrated in the X-ray microscope) and then with a transmission soft X-ray microscope (Mistral Beamline, ALBA synchrotron). Based on the FL signal, the cell candidates were selected. Next, 2D images mosaics were acquired to locate the areas for tilt series collection (−65° to 65° at 1° intervals and exposure time per image 1–3 s) at 520 eV photon energy. The tilt series were normalized with the XMIPP 3 software package,[70] and aligned and reconstructed using IMOD.[70,71] Five cells per condition at the minimum were considered for the analysis. A more detailed protocol is provided in ref. 72.

In vivo nPTT studies

All the experiments were conducted in accordance with the European Union directives 63/2010UE and Spanish regulation RD 53/2013. The use of these animals was also approved by the Animal Ethics Committee of the Universidad Autónoma de Madrid. We used 6 to 12-week-old female C57BL/6 mice to induce melanoma, a well-established and widely used tumor model.[73] Melanoma tumors were induced by subcutaneous inoculation of 4 million B16-F10 melanoma cells. The measurements of the tumor volume were obtained daily with a digital caliper. After 5–7 d of tumoral growth, the nPTT was performed by administration of AuNCs and SPE at 806 nm at 1 W cm^{-2} for 4 minutes.

The thermal images were obtained with a FLIR thermocamera and the thermographs were obtained with the commercial software of the same brand (see the previous laser set up section). Temperature was monitored by infrared thermography at the skin surface.

For the ICP-MS study, after 21 days of nPTT the animals were euthanized, and the necropsy was performed for the obtention of the samples for ICP-MS. The digestion of the sample was performed with HNO_3, H_2O_2, and HCl in a Teflon reactor, heated to 90 °C in a heating oven. The digestion solution was diluted with a solution containing HCl and thiourea. The final volume was calculated by weight and weight/volume ratio. Samples were digested with three blanks worked in parallel. The determination of Au was performed in a PerkinElmer Nexion 350d instrument under standard conditions. The calibration was performed with standards prepared from certified standard solutions traceable to NIST. The digested sample was analysed directly.

Results and discussion

Synthesis and physicochemical characterization of gold nanocapsules for photothermal therapy

Photothermal responsive hollow plasmonic gold nanocapsules (AuNCs) were engineered by templating Au seeds onto polystyrene spheres through layer-by-layer (LbL) assembly followed by a silica coating shell, core dissolution, *in situ* gold growth and silica shell removal.[60,66] Transmission-electron micrographs (Fig. 1A and Fig. S1A, B, ESI†) show complete loss of the electron-lucent silica layer while preserving a dense monolayer of ∼10 nm Au nanoparticles, and the outer diameter of the hollow structures remains 400 ± 20 nm, matching the template size. The capsules display intense dark-field scattering with a narrow ensemble peak at 620 nm (Fig. 1B), indicative of good colloidal stability and size homogeneity. Their UV-vis-NIR extinction spectrum is dominated by a broad localised surface-plasmon resonance (LSPR) that extends well into the first biological window[48,49] (700–950 nm) (Fig. 1C; *cf.*, SectionS1 and Fig. S1A, B, ESI†), a signature of strong electromagnetic coupling inside the confined plasmonic shell. The strong plasmonic coupling maximises heat generation (AuNCs' responsiveness) under NIR illumination.

Under 830 nm multiphoton excitation the particles generate bright, concentration- and power-dependent luminescence (*cf.*, SectionS1 and Fig. S1C, ESI†), enabling intrinsic imaging[29] without additional labels. Furthermore, AuNC concentration and 2PE power jointly determine heat generation and killing efficiency in 3D tumorspheres (SectionS2 and Fig. S2A, ESI†). The photothermal efficiency under pulsed 2PE (830 nm, 600 ns 2PE pulses) is a thoroughly discussed qualitatively in the ESI† (Section S2 and Fig. S2A, ESI†). When an aqueous bulk dispersion (50 μg Au mL^{-1}) was irradiated with an 806 nm continuous-wave laser at 1 W cm^{-2}, the temperature rose from 22 °C to 31 °C within six minutes and returned to baseline after the beam was blocked (Fig. 1D). Applying these data to eqn (1) yielded a photothermal conversion efficiency of 37%, comparable to the best values reported for plasmonically coupled Au assemblies and markedly higher than that of isolated 20 nm Au

nanoparticles.[74] The enhanced performance stems from collective plasmon damping and efficient non-radiative decay within the tightly packed Au monolayer.[70]

Beyond their synthetic simplicity, the capsules confer distinct biological advantages. Large (~400 nm) AuNCs are rapidly internalised and progress more slowly through the endo-lysosomal pathway than smaller Au nanoparticles, which prolongs their intracellular residence time and extends the therapeutic window, an effect first demonstrated for polyelectrolyte capsules by Kastl *et al.*[75] Our recent study using 3D melanoma models showed that the hollow cavity can encapsulate fluorescent payloads while the densely packed inner Au nano-islands provide bright two-photon luminescence, enabling simultaneous deep-tissue imaging and heat delivery.[29] Moreover, the NCs efficiently target tumor biomarkers *in vivo*[36] thus enhancing chemotherapeutic availability. Taken together, the structural integrity, broadband NIR absorption, bright multiphoton luminescence, high light-to-heat conversion efficiency, targetability, and biocompatibility, identify these ~400 nm AuNCs as powerful theranostic agents for image-guided photothermal ablation of solid tumours.

Biological characterization of photoresponsive AuNCs in melanoma *in vitro* models

We next evaluated the photothermal performance of AuNCs in oncologically relevant B16-F10 melanoma spheroids.[76] Tumor spheres were incubated with 0.1–80 μg mL^{-1} AuNCs and irradiated for 10 min with two-photon (2P) light at 830 nm at 3, 6, or 12 mW. Twenty-four hours later, live/dead staining and confocal imaging (SPL) revealed a clear, biparametric dependence. Viability decreased monotonically with both nanoparticle dose and laser power, failing to ~48% at 80 μg mL^{-1} and 12 mW (Fig. 2A and B). Two-photon luminescence (2PL, cyan) acquired simultaneously provided an intrinsic, real-time map of AuNC distribution (Fig. 2B). Regions that emitted a lower 2PL signal (*i.e.*, cyan luminescence recorded under identical imaging settings) contained fewer AuNCs and, consequently, experienced weaker inter-particle coupling and less photothermal damage. This result underscores that local particle density, rather than laser fluence alone, determines therapeutic outcome. Three photothermal regimes emerged: (i) high 2PL/high mortality (≥1 μg mL^{-1} AuNCs, 12 mW, 22 × 10^6 W cm^{-2}), (ii) high 2PL/low mortality (10–80 μg mL^{-1}, 6 mW; 11 × 10^6 W cm^{-2}), and (iii) high 2PL/no mortality (10–80 μg mL^{-1}, 3 mW; 5.5 × 10^6 W cm^{-2}). Similar power-dependent 2PL amplification has been reported for thinner AuNC shells,[29] confirming that greater particle loading and stronger excitation synergistically enhance local heating.

To resolve how AuNC-mediated PTT (nPTT) ablates chemoresistant B16-F10 spheroids, we mapped cell viability as a function of nanoparticle dose, laser power and exposure time (Fig. S2A, ESI†). Controls in which either the laser (830 nm, 2PE) or the AuNCs were omitted compromised viability, confirming that all cytotoxicity stemmed from nPTT. Mortality scaled synergistically with both AuNC concentration and irradiation time, defining low (90–60% viability), moderate (60–30% viability) and high (<30% viability) nPTT windows. Unless

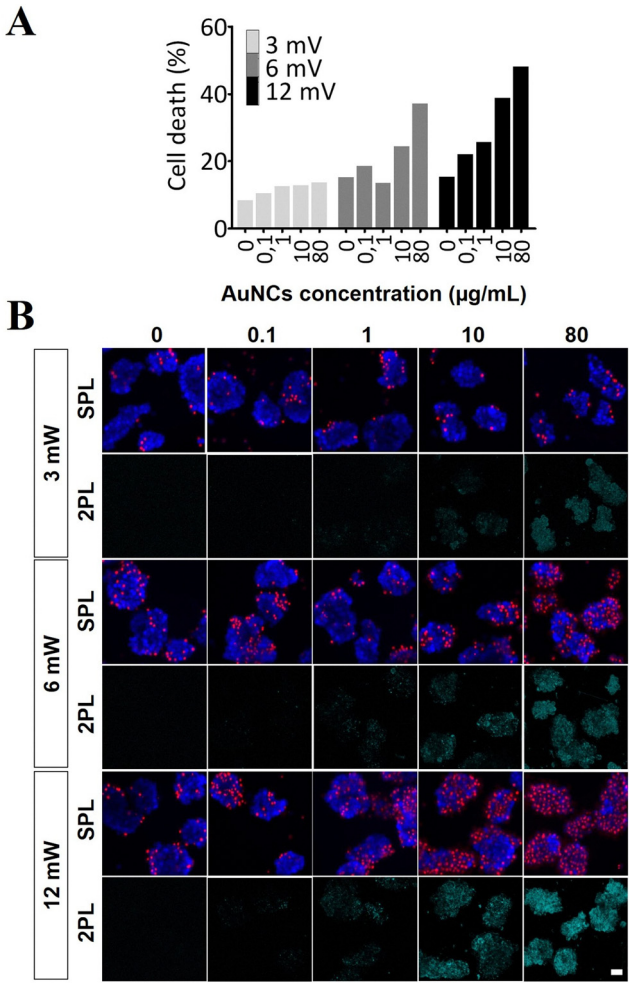

Fig. 2 Imaging-guided two-photon photothermal therapy (2PE-PTT) in B16-F10 melanoma spheroids. (A) Quantitative dose–response of nanoparticle-assisted PTT. Cell death was determined 24 h after a single 2-photon pulse (830 nm, 600 ns) delivered at 3, 6 or 12 mW to spheroids incubated with the indicated concentrations of AuNCs. Values are expressed as the percentage of propidium-iodide-positive nuclei (n = 5 spheroids per condition). (B) Representative confocal maximum-intensity projections acquired 10 min after irradiation. For each laser power (3, 6 and 12 mW) the upper row (SPL) shows single-photon fluorescence channels: live cells stained with CytoCalcein Violet 450 (blue) and dead cells with propidium iodide (red). The lower row (2PL) displays the intrinsic two-photon luminescence (2PL) of the AuNCs (cyan) recorded simultaneously, illustrating nanoparticle distribution within the spheroid core and periphery. Increased particle dose and laser power correlate with a higher cyan signal and a progressive transition from isolated cell death to widespread necrosis. Scale bar, 10 μm.

specified otherwise, subsequent mechanistic experiments were performed under "low-nPTT" conditions, 5 μg mL^{-1} AuNCs, 600 ns pulses at 830 nm, and 3 mW (5.5 × 10^6 W cm^{-2}), which inflict sub-lethal heat stress while preserving overall spheroid architecture. Live/dead imaging after high-nPTT confirmed extensive propidium iodide uptake and membrane poration, indicating that thermoablation proceeds *via* severe plasma membrane damage rather than apoptosis alone.

To benchmark our capsules, we synthesised surfactant-free gold nanostars (AuNSs, ~110 nm, LSPR ≈ 830 nm), known to

be an excellent photosensitive nanomaterial.[77] At equivalent total Au, AuNCs induced higher apoptosis/necrosis than AuNSs (Fig. S2B, ESI†), despite the stronger far-field extinction of the stars. This superiority likely stems from the contiguous, hollow plasmonic layer in AuNCs, which concentrates thermal energy at the particle–cell interface and causes catastrophic membrane damage (Fig. S2C, ESI†). Collectively, these data position AuNCs as a robust 2PL-traceable platform for eradicating chemoresistant melanoma spheroids and for augmenting conventional chemotherapy.

Melanoma spheroids are notoriously chemoresistant because of a drug-efflux-active side-population.[78–82] Consistently, paclitaxel (PTX) at up to 100 μM reduced spheroid viability by only 8% (Fig. S3, ESI†), whereas the same drug was cytotoxic to adherent B16-F10 cells, illustrating the protective effect of the 3D architecture.[29] Importantly, combining low-dose PTX with sub-ablative nPTT (5 μg mL^{-1} AuNCs, 3 mW, 5.5 × 10^6 W cm^{-2}) significantly potentiated cytotoxicity (Fig. S4, ESI†), mirroring the chemo-photothermal synergy described for other plasmonic constructs.[83]

Together, these data establish AuNCs as a potent, 2PL-traceable platform for eradicating chemoresistant melanoma spheroids and potentiating chemotherapy.

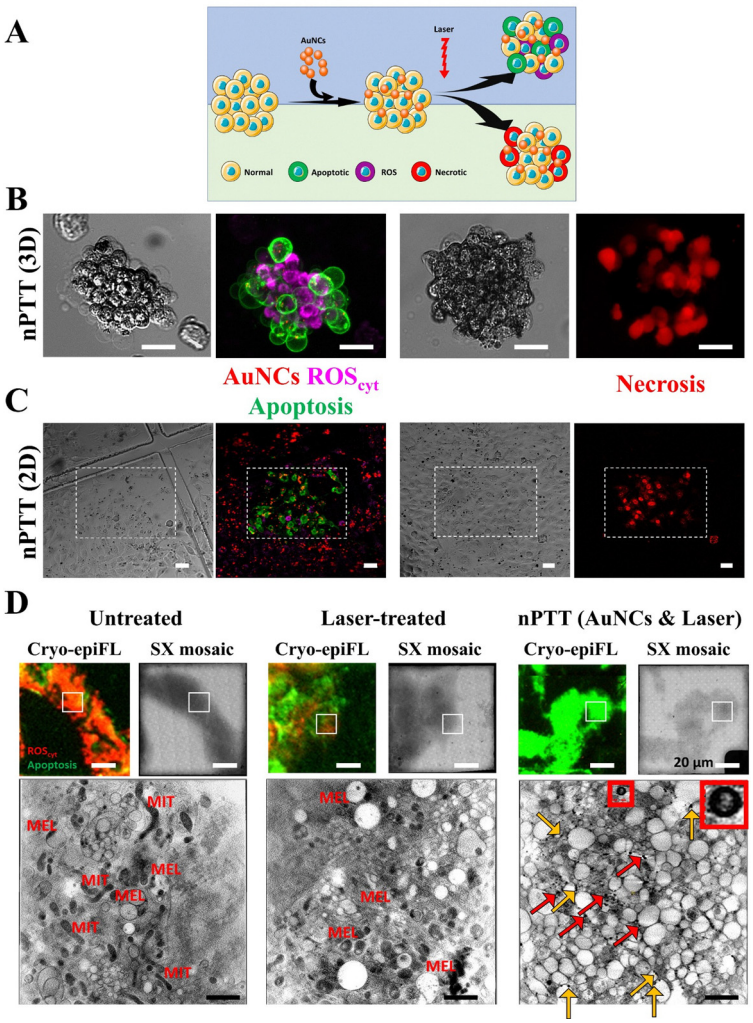

Fig. 3 Cellular response to AuNC-mediated PTT in 3D and 2D B16-F10 melanoma models. (A) Schematic representation of the experimental workflow: Au nanocapsules (AuNCs) are internalised into B16-F10 cells and irradiated with two-photon excitation (2PE), inducing differential cell death pathways. (B) Confocal micrographs of 3D spheroids 10 min post-nPTT, showing induction of apoptosis (green, phosphatidylserine (PS) externalisation), cytoplasmic reactive oxygen species (ROScyt, magenta), and necrosis (red, propidium iodide (PI) nuclear uptake). Scale bar: 10 μm. (C) Representative 2D cultures subjected to the same treatment reveal similar activation of apoptotic, oxidative, and necrotic pathways. Scale bar: 10 μm. (D) Cryo-epifluorescence (Cryo-epiFL) and soft X-ray tomography (SX) of 2D cultures under three conditions: untreated, laser-only, and combined AuNC plus laser treatment (nPTT). Virtual slices (bottom) show intracellular structures including mitochondria (MIT) and melanosome-like vesicles (MEL). In the nPTT group, AuNCs are visualised as dense inclusions (red arrows), and membrane perforations are evident (yellow arrows). The insets highlight intact capsules and fragmented Au debris. Scale bars: top panels, 20 μm; bottom panels, 2 μm. Abbreviations: AuNCs, gold nanocapsules; PTT, photothermal therapy; 2PE, two-photon excitation; PS, phosphatidylserine; PI, propidium iodide; ROScyt, cytoplasmic reactive oxygen species; Cryo-epiFL, cryo-epifluorescence; SX, soft X-ray; MIT, mitochondria; MEL, melanosome-like vesicle.

nPTT induces rapid oxidative stress and membrane destabilization in B16-F10 melanoma models

To evaluate the mechanisms of cell death triggered by nPTT, we monitored B16-F10 melanoma spheroids using live-cell and high-resolution imaging modalities, as outlined in Fig. 3A. Rhodamine B-loaded AuNCs were used to track nanoparticle distribution (λ_{ex} = 543 nm). Coupled with RhB's minimal absorbance at 830 nm ($\varepsilon < \varepsilon < 20\ M^{-1}\ cm^{-1}$) and the viability observed in control spheroids (Fig. 3D and Fig. S6, ESI;† ref. 84), these findings exclude RhB-induced phototoxicity and demonstrate that cytotoxicity stems solely from the photothermal action of the Au shells.

Upon treatment with 30 μg mL^{-1} AuNCs and 2PE irradiation (830 nm, 3 mW (5.5×10^6 W cm^{-2}), 10 min), we observed marked cell death in 3D spheroids (Fig. 3B) and 2D cultures (Fig. 3C). In both models, nPTT induced phosphatidylserine (PS) externalization (green) and strong propidium iodide (PI) nuclear staining (red), indicative of apoptosis and necrosis, respectively. In parallel, cytoplasmic ROS (ROScyt) accumulation was detected shortly after nPTT in both 3D and 2D cultures (magenta, Fig. 3B, C and Fig. S5, ESI†). Control spheroids displayed negligible ROS levels and no PS signal (Fig. S5A, ESI†), while ROScyt increased sharply within 5 min post-nPTT (Fig. S5B, ESI†), preceding the onset of PS positivity and morphological swelling. Notably, once cells became apoptotic, ROScyt levels did not continue to rise, suggesting that oxidative stress may act as a trigger rather than a consequence of apoptosis. The high PS signal detected just 10 min after irradiation could also reflect increased plasma membrane permeability, rather than *de novo* apoptosis, as PS probes may more easily diffuse into the cytosol under membrane-disruptive conditions. This is consistent with literature describing pore formation and local membrane destabilization because of rapid, confined heating.[85–87] Furthermore, given the intrinsic photocatalytic activity of gold nanostructures, the possibility of a combined photothermal and photodynamic effect cannot be excluded.[51,88–92]

To investigate subcellular effects in more detail, we used cryo-correlative epifluorescence (Cryo-epiFL) and soft X-ray tomography (cryoSXT). This is an imaging approach that allows analyzing the 3D cartography of a cell in its native state at organelle resolution level.[71,72] The high electron density of AuNCs enables their use as contrast agents. With this approach, we assessed the cellular architecture under mild nPTT conditions (30 μg mL^{-1} AuNCs, 830 nm, 3 mW, 5.5×10^6 W cm^{-2}), where gross viability remains largely intact (Fig. 3D). While untreated and laser-only cells showed normal ultrastructure, the nPTT group exhibited plasma membrane perforation, AuNC decomposition, and the loss of cytoplasmic and nuclear components. Red arrows denote electron-dense Au debris, while yellow arrows highlight membrane pores of approximately 1–1.5 μm (Fig. S6, ESI†). A close inspection of the virtual tomograms therefore points to early membrane rupture and *in situ* AuNC disintegration, phenomena that require transient local temperatures exceeding the 45–50 °C threshold for lipid bilayer melting and protein denaturation.[49,93,94] Cryo-epiFL imaging of these samples confirmed massive PS exposure and the apparent absence of ROScyt, likely due to leakage of the ROS probe through permeabilized membranes.

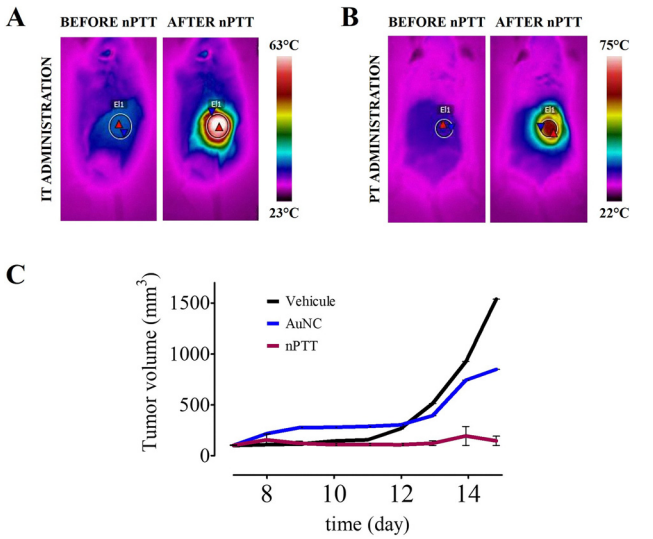

Fig. 4 *In vivo* thermography and therapeutic outcome of AuNC-assisted photothermal therapy. (A) IT injection. Representative infrared images taken immediately before and after a single 4-min NIR exposure (806 nm, 1 W cm^{-2}). The region of interest (E1) reaches a peak surface temperature of 64 °C (color scale 23–63 °C). (B) PT injection. The same imaging sequence for a mouse receiving four peri-lesional AuNC deposits. Heating is confined to the tumor rim, with a peak surface temperature of 62 °C (color scale 22–75 °C). (C) Tumour-volume evolution (mean ± SD, n = 5) after three treatments: Vehicle (IT saline), AuNCs (IT AuNCs, no laser) and nPTT (IT AuNCs followed 24 h later by NIR irradiation). Abbreviations: AuNCs, gold nanocapsules; nPTT, nanoparticle-assisted photothermal therapy; IT, intratumoural; PT, peritumoural.

Collectively, these observations support a model in which nPTT triggers inside-out hyperthermia, a highly localized heating mechanism that rapidly destabilizes the plasma membrane. This mechanism mirrors the membrane-rupturing activity observed in magnetic hyperthermia with iron oxide nanoparticles and may help circumvent chemoresistance by increasing drug access to the intracellular space.

Intratumoral AuNCs drive uniform cytotoxic hyperthermia and durable B16-F10 melanoma remission *in vivo*

Having established the *in vitro* performance of the AuNCs, we next assessed their therapeutic capacity *in vivo* using B16-F10 melanoma xenografts in C57BL/6 mice.[95] Tumours were treated once they reached ~100 mm^3 (12–14 days post-inoculation). AuNCs (1 mg; 28.5 mg mL^{-1}) were injected either intratumourally (IT) one bolus into the tumour core, or peritumorally (PT), four deposits circumscribing the lesion. In both cases the AuNCs were allowed to diffuse for 24 h; shorter distribution times (1 h) produced heterogeneous heating and tumour relapse (data not shown). We treated each tumor with a single 4-min laser irradiation (806 nm laser, 1 W cm^{-2}) (treatment procedure shown in Fig. S7, ESI†).

Real-time thermography showed surface temperatures rising to ~55 °C in AuNC-laden tumors, compared with sub-lethal

<38 °C in laser-only controls (Fig. S8, ESI†). At the end of irradiation, the surface temperature of IT-treated lesions reached 64 °C, whereas PT-treated lesions peaked at 62 °C. In both cases the minimum temperature within the heated area was ≈55–56 °C, yielding a nearly identical ΔT of ≈26 °C (Fig. 4A and B; sequences in Fig. S9 and S10 (ESI†), quantitative summary in Table S1, ESI†). Because conductive losses typically reduce the IT temperature by 8–12 °C,[96,97] the bulk of the tumor was held at 45–50 °C for at least the final minutes of irradiation, which is well within the cytotoxic hyperthermia window (≥43 °C maintained for ≥4 min).[98,99]

Despite similar surface profiles, therapeutic outcome diverged markedly. IT-nPTT eradicated every tumor, with volumes regressing to an imperceptible scar over the 21-day observation period (Fig. 4C and Table S1, ESI†). In contrast, PT-nPTT produced a striking superficial hot-spot but left a viable core that later resumed growth. The difference arises from nanoparticle distribution, rather than peak surface temperature. PT injection concentrates AuNCs near the skin, photon absorption occurs there, thus creating a steep gradient (hot rim → cool core) that spares deeper cells. Conversely, IT delivery disperses them throughout the parenchyma, ensuring the entire tumor volume absorbs sufficient heat, thus enabling uniform heat deposition for irreversible damage, and sparing the overlying skin from visible thermal injury.

This behavior agrees with other reports in which tightly clustered gold nanoparticles convert light to heat efficiently and that homogeneous intratumoral coverage is critical for cure. Examples include polyethyleneimine-induced AuNP clusters that eradicate CT26 tumours under 680 nm irradiation,[100] Au nanorod/glutathione-Au-cluster hybrids that outperform single rods against HeLa cells,[101] and 5-fluorouracil-templated Au clusters that enhance immunogenic hyperthermia in colorectal carcinomatosis.[102] The densely packed inner shell of our AuNCs (Fig. 1A) provides an analogous architecture, underscoring their suitability for single-session photothermal eradication of melanoma.

No off-target burns, weight loss, or behavioural changes were observed, underscoring the safety of a single, image-guided AuNC injection followed by short NIR irradiation. Taken together, the data in Fig. 4 and the supporting thermographic analyses (Fig. S7 to S10 and Table S1, ESI†) show that an optimized IT protocol with AuNCs produces homogeneous cytotoxic hyperthermia (≈45–50 °C intratumorally) and achieves durable control of aggressive melanoma in a single session, setting the stage for the biodistribution and fragmentation-driven clearance analysis of AuNCs presented next.

Gold biodistribution after nPTT is dictated by the injection route

To elucidate the *in vivo* fate of the contrast agent and its relationship to therapeutic efficacy, we quantified elemental gold 24 h after treatment using ICP-MS (Fig. 5 and Fig. S11, ESI†). The technique vaporises and ionises the sample, then separates mono-charged ions by mass, allowing ppb-level metal quantification.[103] In the IT group (Fig. 5A) only ≈4% of the injected dose was recoverable and >99% of that resided in the post-treatment scar. Although no charring was visible at the time of irradiation, a haemorrhagic scab formed within 24 h, evidence of sub-cutaneous necrosis caused by the transient 45–50 °C IT temperature rise. Liver, spleen and kidney together contained <0.05% of the dose, indicating minimal systemic dissemination.

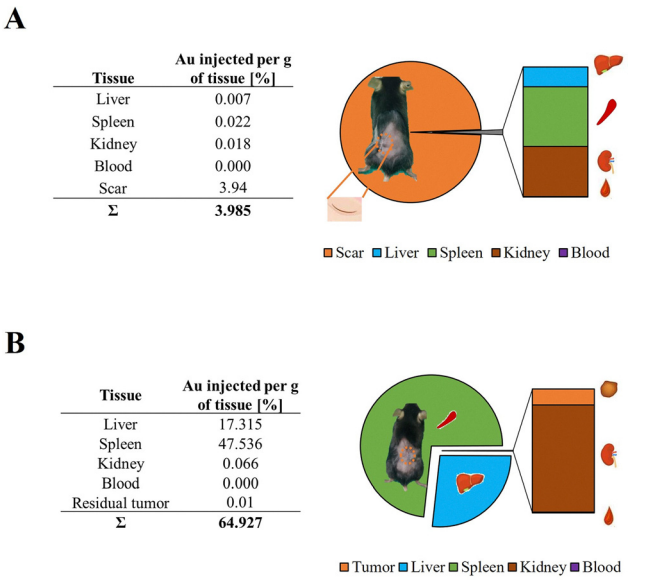

Fig. 5 Biodistribution of gold after AuNC-mediated photothermal therapy. (A) IT route. B16-F10 tumours (day 5) received 1 mg of AuNCs directly into the tumour core and were irradiated 24 h later with an 806 nm laser (4 min, 1 W cm^{-2}), reaching a peak surface temperature of 64 °C. ICP-MS performed 24 h post-irradiation shows that >99% of the detected gold remains confined to the residual scar, with negligible uptake by the liver, spleen or kidneys. (B) PT route. An identical tumour received the same AuNC dose in four peri-lesional deposits; after 24 h diffusion the same laser protocol produced a peak surface temperature of 62 °C. In contrast to the IT group, most of the gold redistributed systemically, accumulating predominantly in the spleen (≈48% of measured gold) and liver (≈17%), with only traces in the residual tumour remnant. Abbreviations: AuNCs, gold nanocapsules; nPTT, nanoparticle-assisted photothermal therapy; IT, intratumoural; PT, peritumoural; ICP-MS, inductively coupled plasma mass spectrometry.

The pattern was reversed after PT administration (Fig. 5B). ≈65% of the dose was still detectable, but only 0.01% remained in the residual tumour; no scar formed, consistent with the superficial heating profile. Instead, gold accumulated in the spleen (48%) and liver (17%), classical sinks of the mononuclear phagocyte system. The large (∼400 nm) intact AuNCs injected around the lesion likely entered the leaky peritumoral vasculature and were rapidly cleared by circulating and resident macrophages, whereas those delivered intratumorally became trapped within the irregular melanoma vasculature[104] or immobilised in the necrotic scar.

A trace kidney signal (0.02–0.07% in both groups) indicates that laser heating fragmented a small fraction of AuNCs into sub-6 nm debris capable of glomerular filtration. Such shock-wave-driven disassembly of plasmonic nanoparticles under nanosecond pulses has been reported previously[41,105] and is

corroborated here by cryo-SXT, which shows sub-10 nm shards dispersed in the cell cytoplasm (Fig. 3 and Fig. S11, ESI†).

Taken together, the data indicate that the injection route dictates AuNC retention *versus* systemic clearance. Although the PT route leaves ~65% of the injected gold in the spleen and liver, prior studies show that comparable hepatic/splenic burdens of dextran-coated 20–30 nm AuNPs cause no histopathological changes or elevations in AST, ALT, creatinine or pro-inflammatory cytokines up to 4 weeks post-exposure.[63] Likewise, transient IL-6 and TNF-α spikes reported for intravenously delivered gold colloids normalise within 96 h, suggesting a self-limited innate response. In our study, animals exhibited normal behaviour, weight gain and grooming throughout the 21-day follow-up, further indicating an absence of overt toxicity. Nevertheless, long-term (≥3-month) studies with comprehensive serum chemistry and organ histology are warranted to definitively rule out chronic effects. IT administration confines most gold, both intact AuNCs and photothermally generated fragments, to the treatment site, explaining the uniform deep heating and complete tumour ablation. PT delivery enables widespread escape, reducing IT gold concentration, limiting heating at depth, and ultimately permitting tumour regrowth. The small but consistent renal signal in both groups further suggests that photothermal fragmentation generates ultra-small gold species that can be renally excreted, consistent with the size-dependent urinary clearance threshold (<6 nm) reported by Choi *et al.*[103] Thus, nanoparticle retention, rather than the total injected dose, emerges as the decisive factor for durable photothermal tumour control, while laser-induced fragmentation provides a plausible pathway for long-term elimination of residual gold from the body.

Conclusions

In this study, we demonstrated for the first time that the plasmonic photoresponsive properties of AuNCs can be exploited for two-photon luminescence-assisted nPTT. We validated AuNCs as an effective photothermal probe using paclitaxel-resistant B16-F10 melanoma spheroids, a three-dimensional model of chemoresistant melanoma. AuNCs alone were biocompatible with no measurable cytotoxicity in spheroids, consistent with prior reports on similar nanocapsules. Under two-photon excitation at 830 nm, AuNCs produced bright luminescence and efficient heat generation, with both signals increasing as AuNC concentration and laser power were increased (up to an optimal 80 μg mL^{-1} and 12 mW). This photothermal effect led to significant melanoma cell ablation *in vitro*. Notably, at equivalent gold doses, AuNCs outperformed gold nanostars, an established photothermal agent, in treating chemoresistant melanoma spheroids. Correlative epifluorescence imaging and cryo-soft X-ray microscopy confirmed that AuNCs disintegrated under these laser treatment conditions and induced nanoscale pores in cell membranes. We also observed elevated ROS during AuNC phototherapy, suggesting a combined photothermal and photodynamic mechanism of cancer cell killing. *In vivo* results further underscore the promise of this approach. In a murine subcutaneous melanoma model, AuNC-mediated PTT yielded complete tumor elimination with both intratumoral and peritumoral nanoparticle administration. However, the route of administration significantly influenced AuNC biodistribution. Intratumoral injection followed by PTT caused a localized necrotic tumor scab that effectively sequestered the bulk of the nanoparticles at the treatment site, limiting their spread. As a result, gold from intratumoral therapy remained largely at the tumor and was shed with the scab, with only minimal traces detected in the liver and spleen. By contrast, peritumoral injection (where no necrotic scab formed) still achieved tumor clearance but allowed more AuNCs to enter circulation, leading to appreciable gold accumulation in off-target organs such as the spleen and liver after treatment. In the intratumoral treatment scenario, detection of gold in the kidneys indicates that some heat-damaged AuNC fragments became small enough for renal clearance, a favorable outcome for nanoparticle elimination. Overall, our findings highlight AuNCs as a powerful nanoparticle-assisted PTT platform for chemotherapy-resistant melanoma. The ability of these nanocapsules to eradicate tumors under NIR excitation, while largely confining the particles to the tumor site (especially with intratumoral delivery), points to a potentially safer profile compared to many systemic nanotherapies. For clinical translation, the choice of delivery route will be important to balance maximal tumor destruction with minimal systemic exposure. This AuNC-based 2PL-guided phototherapy could be further enhanced by incorporating drug delivery (capitalizing on the AuNCs' cargo-loading capability) or by combining with other treatments. Our study lays the groundwork for advanced two-photon guided chemo-PTT strategies and supports the continued development of AuNCs toward effective, targeted melanoma treatment.

Author contributions

PZP, QS, and HDS performed the experiments. JJC assisted with the measurements at Synchrotron. MCIC, NF and DJ assisted with the *in vivo* experiments. PRG conceived the work, analysed the results, prepared the figures, and wrote the manuscript. All authors reviewed the manuscript.

Conflicts of interest

The authors declare that they have no competing interests.

Ethics approval and consent to participate

All the experiments were conducted in accordance with the European Union directives 63/2010UE and Spanish regulation RD 53/2013. The use of these animals was also approved by the Animal Ethics Committee of the Universidad Autónoma de Madrid (Madrid, Spain).

Abbreviations

AuNCs Gold nanocapsules

CLSM	Confocal laser scanning microscopy
CW	Continuous wave
cryoSXT	Cryo-soft X-ray microscopy
GM	Growth medium
HEDFM	Hyperspectral-enhanced dark field microscopy
ICP-MS	Inductively coupled plasma atomic mass spectrometry
IT	Intratumorally
nPTT	Nanoparticle-assisted photothermal therapy
MPE	Multiphoton excitation
NIR	Near-infrared
2PE	Two-photon excitation
2PL	Two-photo luminescence
PI	Propidium iodide
PS	Phosphatidylserine
PTX	Paclitaxel
PT	Peritumoral
ROS	Reactive oxygen species
ROS_{cyt}	Cytoplasmatic reactive oxygen species
RT	Room temperature
SPL	Single photon luminescence

Data availability

All data generated or analysed during this study are included in this published article (and its ESI†). The supporting information file contains additional information on the methodology and results.

Acknowledgements

The study of the nanophotothermal therapy (nPTT) effects of gold nanocapsules (AuNCs) on melanoma cells using cryo soft X-ray tomography (CSXT) was conducted at the MISTRAL beamline of the ALBA Synchrotron (Project number: 2016091853). PRG acknowledges the Ministry of Science, Innovation and Universities (AEI-PID2022-140423NB-I00/AEI/10.13039/501100011033 and CNS2023 – 143700) and the AGAUR (2021 SGR 00175) for financial support. D. Jaque acknowledges the Ministry of Science, Innovation and Universities of Spain (PID2023-146775OB-I00). The authors thank Dr Vladimir Mulens Arias for fruitful discussions and Alba Riba for her contribution (Fig. S2A, ESI†).

References

1 F. Bray, M. Laversanne, H. Sung, J. Ferlay, R. L. Siegel, I. Soerjomataram and A. Jemal, *Ca-Cancer J. Clin.*, 2024, **74**, 229–263.
2 M. Arnold, D. Singh, M. Laversanne, J. Vignat, S. Vaccarella, F. Meheus, A. E. Cust, E. de Vries, D. C. Whiteman and F. Bray, *JAMA Dermatol.*, 2022, **158**, 495–503.
3 C. Karimkhani, A. C. Green, T. Nijsten, M. A. Weinstock, R. P. Dellavalle, M. Naghavi and C. Fitzmaurice, *Br. J. Dermatol.*, 2017, **177**, 134–140.
4 Y. Sun, Y. Shen, Q. Liu, H. Zhang, L. Jia, Y. Chai, H. Jiang, M. Wu and Y. Li, *J. Am. Acad. Dermatol.*, 2025, **92**, 100–107.
5 Melanoma of the Skin – Cancer Stat Facts, **https://seer.cancer.gov/statfacts/html/melan.html**, (accessed May 13, 2025).
6 J. Larkin, V. Chiarion-Sileni, R. Gonzalez, J.-J. Grob, P. Rutkowski, C. D. Lao, C. L. Cowey, D. Schadendorf, J. Wagstaff, R. Dummer, P. F. Ferrucci, M. Smylie, D. Hogg, A. Hill, I. Márquez-Rodas, J. Haanen, M. Guidoboni, M. Maio, P. Schöffski, M. S. Carlino, C. Lebbé, G. McArthur, P. A. Ascierto, G. A. Daniels, G. V. Long, L. Bastholt, J. I. Rizzo, A. Balogh, A. Moshyk, F. S. Hodi and J. D. Wolchok, *N. Engl. J. Med.*, 2019, **381**, 1535–1546.
7 H. A. Tawbi, D. Schadendorf, E. J. Lipson, P. A. Ascierto, L. Matamala, E. C. Gutiérrez, P. Rutkowski, H. J. Gogas, C. D. Lao, J. J. D. Menezes, S. Dalle, A. Arance, J.-J. Grob, S. Srivastava, M. Abaskharoun, M. Hamilton, S. Keidel, K. L. Simonsen, A. M. Sobiesk, B. Li, F. S. Hodi and G. V. Long, *N. Engl. J. Med.*, 2022, **386**, 24–34.
8 Center for Drug Evaluation and Research, U.S. Food and Drug Administration (FDA).
9 G. V. Long, D. Stroyakovskiy, H. Gogas, E. Levchenko, F. de Braud, J. Larkin, C. Garbe, T. Jouary, A. Hauschild, J. J. Grob, V. Chiarion Sileni, C. Lebbe, M. Mandalà, M. Millward, A. Arance, I. Bondarenko, J. B. A. G. Haanen, J. Hansson, J. Utikal, V. Ferraresi, N. Kovalenko, P. Mohr, V. Probachai, D. Schadendorf, P. Nathan, C. Robert, A. Ribas, D. J. DeMarini, J. G. Irani, M. Casey, D. Ouellet, A.-M. Martin, N. Le, K. Patel and K. Flaherty, *N. Engl. J. Med.*, 2014, **371**, 1877–1888.
10 M. A. Postow, R. Sidlow and M. D. Hellmann, *N. Engl. J. Med.*, 2018, **378**, 158–168.
11 R. D. Issels and M. H. Falk, *Int. J. Hyperthermia*, 2001, **17**, 1–18.
12 N. M. Bleehen, *Br. J. Cancer, Suppl.*, 1982, **5**, 96–100.
13 C.-H. Hou, F.-L. Lin, S.-M. Hou and J.-F. Liu, *Int. J. Mol. Sci.*, 2014, **15**, 17380–17395.
14 T. Mantso, S. Vasileiadis, I. Anestopoulos, G. P. Voulgaridou, E. Lampri, S. Botaitis, E. N. Kontomanolis, C. Simopoulos, G. Goussetis, R. Franco, K. Chlichlia, A. Pappa and M. I. Panayiotidis, *Sci. Rep.*, 2018, **8**, 10724.
15 J. P. Fruehauf and V. Trapp, *Expert Rev. Anticancer Ther.*, 2008, **8**, 1751–1757.
16 H. Zhao, H. Chen, Z. Guo, W. Zhang, H. Yu, Z. Zhuang, H. Zhong and Z. Liu, *Chem. Eng. J.*, 2020, **394**, 124314.
17 X. Duan, C. Chan and W. Lin, *Angew. Chem., Int. Ed.*, 2019, **58**, 670–680.
18 Q. Chen, Q. Hu, E. Dukhovlinova, G. Chen, S. Ahn, C. Wang, E. A. Ogunnaike, F. S. Ligler, G. Dotti and Z. Gu, *Adv. Mater.*, 2019, **31**, 1900192.
19 D. Chang, M. Lim, J. A. C. M. Goos, R. Qiao, Y. Y. Ng, F. M. Mansfeld, M. Jackson, T. P. Davis and M. Kavallaris, *Front. Pharmacol.*, 2018, **2**(9), 831.
20 J. Beik, Z. Abed, F. S. Ghoreishi, S. Hosseini-Nami, S. Mehrzadi, A. Shakeri-Zadeh and S. K. Kamrava, *J. Controlled Release*, 2016, **235**, 205–221.
21 N. R. Datta, H. P. Kok, H. Crezee, U. S. Gaipl and S. Bodis, *Front. Oncol.*, 2020, **12**(10), 819.

22 J. D. Rybka, *Rep Pract Oncol Radiother.*, 2019, **24**, 152–157.
23 L. R. Hirsch, R. J. Stafford, J. A. Bankson, S. R. Sershen, B. Rivera, R. E. Price, J. D. Hazle, N. J. Halas and J. L. West, *Proc. Natl. Acad. Sci. U. S. A.*, 2003, **100**, 13549–13554.
24 J. Li, X. Zhen, Y. Lyu, Y. Jiang, J. Huang and K. Pu, *ACS Nano*, 2018, **12**, 8520–8530.
25 Y. Li, W. Lu, Q. Huang, C. Li and W. Chen, *Nanomedicine*, 2010, **5**, 1161–1171.
26 G. Dacarro, A. Taglietti and P. Pallavicini, *Molecules*, 2018, **23**, 1414.
27 P. Zhao, Y. Xu, W. Ji, S. Zhou, L. Li, L. Qiu, Z. Qian, X. Wang and H. Zhang, *J. Nanobiotechnol.*, 2021, **19**, 181.
28 Y. Zhang, X. Zhan, J. Xiong, S. Peng, W. Huang, R. Joshi, Y. Cai, Y. Liu, R. Li, K. Yuan, N. Zhou and W. Min, *Sci. Rep.*, 2018, **8**, 8720.
29 P. Zamora-Perez, C. Xiao, M. Sanles-Sobrido, M. Rovira-Esteva, J. J. Conesa, V. Mulens-Arias, D. Jaque and P. Rivera-Gil, *Acta Biomater.*, 2022, **142**, 308–319.
30 R. Di Corato, D. Palumberi, R. Marotta, M. Scotto, S. Carregal-Romero, P. Rivera Gil, W. J. Parak and T. Pellegrino, *Small*, 2012, **8**, 2731–2742.
31 P. Singh, P. Haloi, K. Singh, S. Roy, A. Sarkar, S. L. B. R. Choudhary, C. Mohite, S. Chawla, V. B. Konkimalla, P. Sanpui and A. Jaiswal, *ACS Appl. Mater. Interfaces*, 2023, **15**, 39081–39098.
32 L. Li, C. Chen, H. Liu, C. Fu, L. Tan, S. Wang, S. Fu, X. Liu, X. Meng and H. Liu, *Adv. Funct. Mater.*, 2016, **26**, 4252–4261.
33 I. Grabowska-Jadach, D. Kalinowska, M. Drozd and M. Pietrzak, *Biomed. Pharmacother.*, 2019, **111**, 1147–1155.
34 W. Chen, M. Qin, X. Chen, Q. Wang, Z. Zhang and X. Sun, *Theranostics*, 2018, **8**, 2229–2241.
35 A. S. Bear, L. C. Kennedy, J. K. Young, S. K. Perna, J. P. M. Almeida, A. Y. Lin, P. C. Eckels, R. A. Drezek and A. E. Foster, *PLoS One*, 2013, **8**, e69073.
36 R. Xu, N. Martinez-Bosch, F. Rivera-Hueto, V. Mulens-Arias, F. Rubio-Moscardo, J. Javier Conesa, P. Navarro, R. Vicente and P. Rivera-Gil, *J. Drug Targeting*, 2025, **33**, 143–155.
37 X. Huang and M. A. El-Sayed, *J. Adv. Res.*, 2010, **1**, 13–28.
38 Y. Wu, M. R. K. Ali, K. Chen, N. Fang and M. A. El-Sayed, *Nano Today*, 2019, **24**, 120–140.
39 L. A. Austin, M. A. Mackey, E. C. Dreaden and M. A. El-Sayed, *Arch. Toxicol.*, 2014, **88**, 1391–1417.
40 S. Ashraf, B. Pelaz, P. del Pino, M. Carril, A. Escudero, W. J. Parak, M. G. Soliman, Q. Zhang and C. Carrillo-Carrion, in *Light-Responsive Nanostructured Systems for Applications in Nanomedicine*, ed. S. Sortino, Springer International Publishing, Cham, 2016, pp. 169–202.
41 P. Rivera Gil, D. Hühn, L. L. del Mercato, D. Sasse and W. J. Parak, *Pharmacol. Res.*, 2010, **62**, 115–125.
42 S. Carregal-Romero, M. Ochs, P. Rivera-Gil, C. Ganas, A. M. Pavlov, G. B. Sukhorukov and W. J. Parak, *J. Controlled Release*, 2012, **159**, 120–127.
43 P. K. Jain and M. A. El-Sayed, *Chem. Phys. Lett.*, 2010, **487**, 153–164.
44 P. K. Jain, X. Huang, I. H. El-Sayed and M. A. El-Sayed, *Acc. Chem. Res.*, 2008, **41**, 1578–1586.
45 S. Eustis and M. A. El-Sayed, *Chem. Soc. Rev.*, 2006, **35**, 209–217.
46 P. Zamora-Perez, B. Pelaz, D. Tsoutsi, M. G. Soliman, W. J. Parak and P. Rivera-Gil, *Nanoscale*, 2021, **13**, 13256–13272.
47 P. Zamora-Perez, D. Tsoutsi, R. Xu and P. Rivera_Gil, *Materials*, 2018, **11**, 243.
48 E. Hemmer, A. Benayas, F. Légaré and F. Vetrone, *Nanoscale Horiz.*, 2016, **1**, 168–184.
49 D. Jaque, L. M. Maestro, B. del Rosal, P. Haro-Gonzalez, A. Benayas, J. L. Plaza, E. M. Rodríguez and J. G. Solé, *Nanoscale*, 2014, **6**, 9494–9530.
50 Z. Bao, X. Liu, Y. Liu, H. Liu and K. Zhao, *Asian J. Pharm. Sci.*, 2016, **11**, 349–364.
51 V. Guerrero-Florez, S. C. Mendez-Sanchez, O. A. Patrón-Soberano, V. Rodríguez-González, D. Blach and F. Martínez, *J. Mater. Chem. B*, 2020, **8**, 2862–2875.
52 S. Bhana, G. Lin, L. Wang, H. Starring, S. R. Mishra, G. Liu and X. Huang, *ACS Appl. Mater. Interfaces*, 2015, **7**, 11637–11647.
53 R. Vankayala, C.-C. Lin, P. Kalluru, C.-S. Chiang and K. C. Hwang, *Biomaterials*, 2014, **35**, 5527–5538.
54 S. M. H. AL-Jawad, A. A. Taha, M. M. F. Al-Halbosiy and L. F. A. AL-Barram, *Photodiagn. Photodyn. Ther.*, 2018, **21**, 201–210.
55 H. S. Kim and D. Y. Lee, *J. Pharm. Invest.*, 2017, **47**, 19–26.
56 H. S. Kim and D. Y. Lee, *Polymers*, 2018, **10**, 961.
57 R. S. Riley and E. S. Day, *Wiley Interdiscip. Rev.: Nanomed. Nanobiotechnol.*, 2017, **9**(4), DOI: **10.1002/wnan.1449**.
58 Q. Chen, L. Xu, C. Liang, C. Wang, R. Peng and Z. Liu, *Nat. Commun.*, 2016, **7**, 13193.
59 N. Zhang, J. Song, Y. Liu, M. Liu, L. Zhang, D. Sheng, L. Deng, H. Yi, M. Wu, Y. Zheng, Z. Wang and Z. Yang, *J. Controlled Release*, 2019, **306**, 15–28.
60 P. Rivera Gil, C. Vazquez-Vazquez, V. Giannini, M. P. Callao, W. J. Parak, M. A. Correa-Duarte and R. A. Alvarez-Puebla, *Angew. Chem., Int. Ed.*, 2013, **52**, 13694–13698.
61 T. Zhou, R. Vicente and P. Rivera-Gil, *ACS Omega*, 2024, **9**, 42183–42192.
62 C. Xiao, V. Izquierdo-Roca and P. Rivera-Gil, *ACS Mater. Au*, 2023, **3**, 164–175.
63 A. Bailly, F. Correard, A. Popov, G. Tselikov, F. Chaspoul, R. Appay, A. Al-Kattan, A. Kabashim, D. Braguer and M. Esteve, *Sci. Rep.*, 2019, **9**, 12890.
64 E. Alexander and K. W. Leong, *Front. Nanotechnol.*, 2025, **7**, 1512622.
65 X.-D. Zhang, Z. Luo, J. Chen, S. Song, X. Yuan, X. Shen, H. Wang, Y. Sun, K. Gao, L. Zhang, S. Fan, D. T. Leong, M. Guo and J. Xie, *Sci. Rep.*, 2015, **5**, 8669.
66 M. Sanles-Sobrido, W. Exner, L. Rodríguez-Lorenzo, B. Rodríguez-González, M. A. Correa-Duarte, R. A. Álvarez-Puebla and L. M. Liz-Marzán, *J. Am. Chem. Soc.*, 2009, **131**, 2699–2705.

67 C. Xiao, V. Izquierdo-Roca and P. Rivera-Gil, *ACS Mater. Au*, 2023, **3**, 164–175.
68 X. Wang, G. Li, Y. Ding and S. Sun, *RSC Adv.*, 2014, **4**, 30375–30383.
69 D. N. Mastronarde and S. R. Held, *J. Struct. Biol.*, 2017, **197**, 102–113.
70 W. W. Overwijk and N. P. Restifo, *Curr. Protoc. Immunol.*, 2000, **39**, 1–29.
71 R. Carzaniga, M.-C. Domart, L. M. Collinson and E. Duke, *Protoplasma*, 2014, **251**, 449–458.
72 M. Chiappi, J. J. Conesa, E. Pereiro, C. O. S. Sorzano, M. J. Rodríguez, K. Henzler, G. Schneider, F. J. Chichón and J. L. Carrascosa, *J. Nanobiotechnol.*, 2016, **14**, 15.
73 R. A. Odion, Y. Liu and T. Vo-Dinh, *Cancers*, 2022, **14**, 5737.
74 J. Wang, Y. Zhang, N. Jin, C. Mao and M. Yang, *ACS Appl. Mater. Interfaces*, 2019, **11**, 11136–11143.
75 L. Kastl, D. Sasse, V. Wulf, R. Hartmann, J. Mircheski, C. Ranke, S. Carregal-Romero, J. A. Martínez-López, R. Fernández-Chacón, W. J. Parak, H.-P. Elsasser and P. Rivera_Gil, *ACS Nano*, 2013, **7**, 6605–6618.
76 H. Lu and M. H. Stenzel, *Small*, 2018, **14**, 1702858.
77 G. Chandrasekar, K. Mougin, H. Haidara, L. Vidal and E. Gnecco, *Appl. Surf. Sci.*, 2011, **257**, 4175–4179.
78 M. Zanoni, F. Piccinini, C. Arienti, A. Zamagni, S. Santi, R. Polico, A. Bevilacqua and A. Tesei, *Sci. Rep.*, 2016, **6**, 19103.
79 I. F. Hermans, T. W. Chong, M. J. Palmowski, A. L. Harris and V. Cerundolo, *Cancer Res.*, 2003, **63**, 8408–8413.
80 Y. Kalechman, D. L. Longo, R. Catane, A. Shani, M. Albeck and B. Sredni, *Int. J. Cancer*, 2000, **86**, 281–288.
81 A. S. Nunes, A. S. Barros, E. C. Costa, A. F. Moreira and I. J. Correia, *Biotechnol. Bioeng.*, 2019, **116**, 206–226.
82 S. M. Mousavi, M. Zarei, S. A. Hashemi, S. Ramakrishna, W.-H. Chiang, C. W. Lai and A. Gholami, *Drug Metab. Rev.*, 2020, **52**, 299–318.
83 M. Deinavizadeh, A. R. Kiasat, M. Shafiei, M. Sabaeian, R. Mirzajani, S. M. Zahraei, F. Khalili, M. Shao, A. Wu, P. Makvandi and N. Hooshmand, *Sci. Rep.*, 2024, **14**, 4373.
84 P. Zamora-Perez, C. Xiao, M. Sanles-Sobrido, M. Rovira-Esteva, J. J. Conesa, V. Mulens-Arias, D. Jaque and P. Rivera-Gil, *Acta Biomater.*, 2022, **142**, 308–319.
85 R. R. Letfullin, C. Joenathan, T. F. George and V. P. Zharov, *Nanomedicine*, 2006, **1**, 473–480.
86 X. Wang, X. Lu, R. Zhu, K. Zhang, S. Li, Z. Chen and L. Li, *Neurochem. Res.*, 2017, **42**, 1130–1140.
87 D. K. Chatterjee, P. Diagaradjane and S. Krishnan, *Ther. Delivery*, 2011, **2**, 1001–1014.
88 S. Hwang, J. Nam, S. Jung, J. Song, H. Doh and S. Kim, *Nanomedicine*, 2014, **9**, 2003–2022.
89 R. S. Riley and E. S. Day, *WIREs Nanomed. Nanobiotechnol.*, 2017, **9**, e1449.
90 L. Minai, D. Yeheskely-Hayon and D. Yelin, *Sci. Rep.*, 2013, **3**, 2146.
91 A. Manke, L. Wang and Y. Rojanasakul, *BioMed Res. Int.*, 2013, e942916.
92 L. Cui, W. Bu, J. Song, L. Feng, T. Xu, D. Liu, W. Ding, J. Wang, C. Li, B. Ma, Y. Luo, Z. Jiang, C. Wang, J. Chen, J. Hou, H. Yan, L. Yang and X. Jia, *Arch. Pharm. Res.*, 2018, **41**, 299–313.
93 H. D. A. Santos, E. C. Ximendes, M. del, C. Iglesias-de la Cruz, I. Chaves-Coira, B. del Rosal, C. Jacinto, L. Monge, I. Rubia-Rodríguez, D. Ortega, S. Mateos, J. GarcíaSolé, D. Jaque and N. Fernández, *Adv. Funct. Mater.*, 2018, **28**, 1803924.
94 B. Sanz, M. P. Calatayud, T. E. Torres, M. L. Fanarraga, M. R. Ibarra and G. F. Goya, *Biomaterials*, 2017, **114**, 62–70.
95 V. Mulens-Arias, A. Nicolás-Boluda, A. Gehanno, A. Balfourier, F. Carn and F. Gazeau, *Nanoscale*, 2019, **11**, 3344–3359.
96 D. Kim, J. Paik and H. Kim, *Sci. Rep.*, 2023, **13**, 12135.
97 M. M. Rahman, I. Pop and M. Z. Saghir, *Int. J. Heat Mass Transfer*, 2019, **129**, 198–211.
98 Z. A. Shahabad, C. B. Avci, F. Bani, A. Zarebkohan, M. Sadeghizadeh, R. Salehi, M. Ghafarkhani, R. Rahbarghazi, B. G. Bagca and N. P. Ozates, *Sci. Rep.*, 2022, **12**, 11774.
99 B. E. Kennedy, E. B. Noftall, C. Dean, A. Roth, K. N. Clark, D. Rowles, K. Singh, L. Pagliaro and C. A. Giacomantonio, *Front. Immunol.*, 2025, **15**, 1512543.
100 S. Liu, J. Wang, Y. Song, S. He and H. Tan, *Pharmaceutics*, 2022, **14**, 2451.
101 V. Mulens-Arias, A. Nicolás-Boluda, A. Pinto, A. Balfourier, F. Carn, A. K. A. Silva, M. Pocard and F. Gazeau, *ACS Nano*, 2021, **15**, 3330–3348.
102 E. C. Mazarakioti, A. Zotos, A.-A. Thomatou, A. Kontogeorgos, A. Patakas and A. Ladavos, *Foods*, 2022, **11**, 3705.
103 H. S. Choi, W. Liu, P. Misra, E. Tanaka, J. P. Zimmer, B. I. Ipe, M. G. Bawendi and J. V. Frangioni, *Nat. Biotechnol.*, 2007, **25**, 1165–1170.
104 W. Ngo, S. Ahmed, C. Blackadar, B. Bussin, Q. Ji, S. M. Mladjenovic, Z. Sepahi and W. C. W. Chan, *Adv. Drug Delivery Rev.*, 2022, **185**, 114238.
105 R. R. Letfullin, C. Joenathan, T. F. George and V. P. Zharov, *Nanomedicine*, 2006, **1**, 473–480.